



Cite this: *Phys. Chem. Chem. Phys.*,
2018, 20, 19606

Role of transition metals in a charge transfer mechanism and oxygen removal in $\text{Li}_{1.17}\text{Ni}_{0.17}\text{Mn}_{0.5}\text{Co}_{0.17}\text{O}_2$: experimental and first-principles analysis†

Tanmay Sarkar,^{abc} Kunkanadu R. Prakasha,^{bc} Mridula Dixit Bharadwaj^a and Annigere S. Prakash^{ib}★^c

Oxygen removal from high capacity Li-rich layered oxide $\text{Li}_{1.17}\text{Ni}_{0.17}\text{Mn}_{0.5}\text{Co}_{0.17}\text{O}_2$ affects the charge transfer process during cycling. During de-lithiation, oxygen removal takes place with the reduction in oxygen binding energy. Co substitution affects oxygen removal by shifting the O-p orbital closer to the Fermi energy. A convex hull plot is used to analyse single-phase and two-phase reactions during de-lithiation in $\text{Li}_{1.17}\text{Ni}_{0.17}\text{Mn}_{0.5}\text{Co}_{0.17}\text{O}_2$ and Li_2MnO_3 . Experimentally, the single-phase and two-phase reactions are identified based on the characteristics of the charge curve. In the charge transfer process more than 80% of lithium charge is transferred to oxygen in both the compounds. Effective charge and cyclic voltammetry reveal the redox centers in the compounds which help to understand the role of oxygen and transition metals in de-lithiation. A detailed explanation of oxygen removal and the charge transfer mechanism of $\text{Li}_{1.17}\text{Ni}_{0.17}\text{Mn}_{0.5}\text{Co}_{0.17}\text{O}_2$ and Li_2MnO_3 is provided in the current experimental and density functional theory based study.

Received 17th May 2018,
Accepted 28th June 2018

DOI: 10.1039/c8cp03148g

rsc.li/pccp

In search of efficient cathode materials for high energy and power density requirements of electric vehicles (EV), Li-rich layered oxides are considered to be a feasible solution owing to their high specific capacity ($\sim 250 \text{ mA h g}^{-1}$).^{1–4} However, there are several challenges associated with the performance of these materials such as (i) high irreversible capacity loss with oxygen removal in the first charge,² (ii) low discharge rate capability,⁵ (iii) capacity fade over cycles,⁵ (iv) low electronic conductivity,^{6,7} and (v) inevitable phase transformation from a layered to spinel phase during cycling,⁸ which undermine the commercial progress of the material.

The origin of most of these challenges associates with the initial activation of the material, which needs further in-depth electronic level analysis. Although Density Functional Theory (DFT) based studies on Li-rich cathodes are reported in the literature they are limited to one or two 3d metals^{9–13} except for the study on $\text{Li}_{1.2}\text{Ni}_{0.13}\text{Fe}_{0.13}\text{Mn}_{0.54}\text{O}_2$ by Laisa *et al.*¹⁴ Dianat *et al.*¹⁵ studied the electrochemical properties like structural

stability, electrochemical potential and Li-ion diffusivity in $\text{Li}[\text{Li}_{1/6}\text{Al}_{1/6}\text{Mn}_{1/2}\text{Ni}_{1/6}]\text{O}_2$. However, none of these studies addressed the electronic origin of the charge transfer process and oxygen removal in Li-rich cathodes involving Ni-Mn-Co. Among them, $\text{Li}_{1.17}\text{Ni}_{0.17}\text{Mn}_{0.5}\text{Co}_{0.17}\text{O}_2$ (LNMC) is considered one of the most promising cathode materials. In LNMC, the presence of Co increases the reversible capacity, but it suffers from O removal which may occur due to the overlap of the Co-d and O-p bands.¹⁶ To address this issue Xiao *et al.*¹⁷ have performed theoretical calculations on $\text{Li}[\text{Li}_{1/3}\text{X}_{2/3}]\text{O}_2$ (X = Mn, Ni, Co, and Ti) and reported that the Co phase reduces the band gap which facilitates oxygen loss. However, such studies are to be extended to LNMC where the presence of multiple transition elements alters the electronic structure of the compounds and hence a systematic approach of first principles calculations together with experimental analysis is required.

In the present study, first principles calculations based on DFT have been used to understand the electrochemical properties of Li-rich LNMC. The theoretical and experimental findings provide new physical insights into the electrochemical performance of LNMC, which is then compared with that of Li_2MnO_3 (LMO). In the proposed work, different phases are analysed with the help of a convex hull plot while charging. Electrochemical performance is analysed based on the following – (a) atomic arrangement in the metal layer, (b) stable phases attained on de-lithiation, (c) voltage profile,

^a Center for Study of Science, Technology and Policy (CSTEP), Bangalore 560094, India

^b Academy of Scientific and Innovative Research (AcSIR), CSIR Madras Complex, Chennai 600113, India

^c CSIR Central Electrochemical Research Institute, Chennai Unit, Chennai 600113, India. E-mail: prakash.as@gmail.com, prakash@cecri.res.in

† Electronic supplementary information (ESI) available. See DOI: 10.1039/c8cp03148g

(d) oxygen removal, (e) Bader method,¹⁸ and (f) density of states (DOS) analysis.

1 Experimental and computational details

Both LMO and LNMC powders were prepared by a two-step method: the microspherical transition metals' carbonate prepared by a hydrothermal method and subsequent annealing-induced lithiation process.

In the first step, a stoichiometric amount of transition metal acetates were dissolved in a mixed solution of ethanol and distilled water (volume ratio of water to ethanol was 2 : 1). Then a required amount of urea was added to the solution which serves as a carbonate source. The mixed solution was sealed in an autoclave and placed in an oven at 200 °C for 36 h followed by slow cooling to room temperature. The precipitate was washed several times with distilled water and then filtered and dried overnight at 80 °C. In the second step the as-prepared carbonate was mixed with stoichiometric lithium hydroxide and sintered at 800 °C for 12 h.

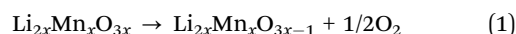
The phase characterization of synthesized materials was carried out by powder X-ray diffraction using a Bruker D8 Advance Diffractometer equipped with a Cu K α source ($1\lambda = 1.54056$ Å, $2\lambda = 1.54439$ Å). Rietveld fits of individual diffraction patterns were carried out using the Fullprof suite program. The morphological features and elemental compositions of both the powder samples were analysed using a Field Emission Scanning Electron Microscope (FESEM MIRA3 LMU) equipped with Oxford X-Max20 energy-dispersive X-ray (EDX). The chemical valence of elements in the sample was measured by X-ray photoelectron spectroscopy (XPS) using a Thermo Fisher Scientific Multilab-2000 spectrometer fitted with non-monochromatic Al K α radiation (1486.6 eV).

Electrochemical studies were performed on Swagelok-type Li half-cells assembled in an argon-filled glovebox. The positive electrodes were prepared by casting a mixture of 80 wt% of active materials, 15 wt% of Super-P Carbon (Timcal Belgium), and 5 wt% of polyvinylidene fluoride using the *N*-methyl-2-pyrrolidinone (NMP) solvent on aluminum foil and dried overnight at 80 °C in a vacuum oven. A metallic lithium disc (Alfa Aesar)

was used as a negative electrode. The electrolyte solution used was 1 M LiPF₆ dissolved in a mixture of ethylene carbonate and dimethyl carbonate and the weight ratio of these carbonates was 1 : 1. A Whatman glass microfiber filter paper was used as a separator. The galvanostatic charge–discharge performance was measured between 2–4.8 V (*versus* Li) in galvanostatic mode using a VMP3Z (Biologic) multichannel potentiostat/galvanostat. The typical cells contained around 4–6 mg cm^{−2} cathode materials.

DFT+*U* based first principles calculations were carried out using the Vienna *ab-initio* Simulation Package (VASP).¹⁹ Perdew–Burke–Ernzerhof (PBE) type Generalized Gradient Approximations (GGA)²⁰ were considered to approximate the exchange and correlation energy. In the simulation, a supercell of $2 \times 1 \times 1$ was considered to reduce the influence under periodic boundary conditions. Further plane wave energy cutoff of 520 eV and *k*-mesh grids of $4 \times 2 \times 4$ (Monkhorst–Pack²¹) were used. In the optimization process, on-site correlation of d-orbitals was incorporated to avoid delocalization using the Hubbard *U* parameter. The *U*-values for Mn (5.0), Ni (5.96) and Co (5.1) were used as reported by Xiao *et al.*¹⁷ For all the calculations, cell parameters and ionic positions were optimized till the force on each atom is <0.01 eV Å^{−1}.

The partial intercalation potentials of studied phases were calculated using the Nernst equation.²² Oxygen binding energy in different compounds is a direct indication of oxygen stability. The binding energy is calculated from the energy obtained during the following reaction.¹⁷



To calculate the binding energy, an oxygen vacancy concentration of 8.3% was considered for all the studied compositions. Weak bonding between metal and oxygen makes the removal of oxygen from the structure easy.

2 Results and discussion

2.1 Structure and morphology

Fig. 1 shows the Rietveld refinement fitting of powder X-ray diffraction patterns of both LMO and LNMC samples. For the

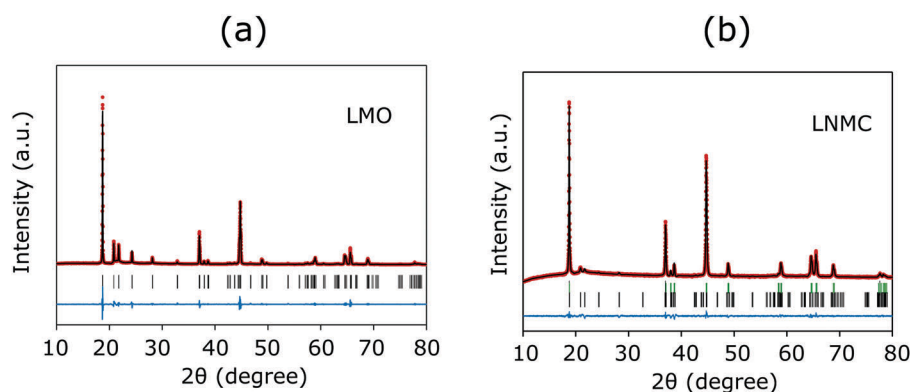


Fig. 1 Rietveld refinement of powder X-ray diffraction patterns of both (a) Li₂MnO₃ and (b) Li_{1.17}Ni_{0.17}Mn_{0.5}Co_{0.17}O₂ phases showing the experimental data points (red), calculated patterns (black), their differences (blue) and Bragg diffraction positions (black ticks for *C2/m* and green sticks for *R3m* space group).

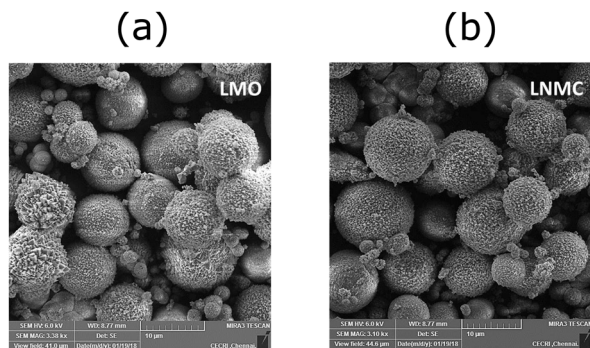


Fig. 2 FESEM images of (a) Li_2MnO_3 and (b) $\text{Li}_{1.17}\text{Ni}_{0.17}\text{Mn}_{0.5}\text{Co}_{0.17}\text{O}_2$ powder samples.

refinement of the LMO phase a monoclinic system with a $C2/m$ space group is used whereas a two phase model (monoclinic system with a space group of $C2/m$ and rhombohedral system with a space group of $R\bar{3}m$) was used for LNMC. The clear splitting of two peaks around $65\text{--}70^\circ$ for both the samples suggests the well-ordered layered structure.^{23,24} The obtained crystallographic parameters are summarized in Tables S1 and S2 in the ESI† Fig. 2a and b show FESEM images of the LMO and LNMC particles which are fused tightly into polycrystalline spherical agglomerates with sizes of $5\text{--}15\text{ }\mu\text{m}$.

2.2 Optimization of ground state structure

LMO has a layered structure similar to LiMO_2 ($\text{M} = \text{Co}, \text{Mn}$, and Ni) with ABC oxygen stacking and additional Li in the Mn layer. In the structure, one additional Li ion per two Mn ions is positioned in the 2b Wyckoff site and formed the LiM_2 layer. The initial crystallographic information of LMO from the ICSD has been used for total energy calculations to optimize the ground state structure.²⁵ The same crystallographic information has been used to construct the unit cell of LNMC,

where two atoms of Mn and Li are replaced with Ni and Co atoms in the LiM_2 layer.

In LNMC, different atomic positions of Li, Co, Mn, and Ni in the LiM_2 plane are considered to obtain the ground state structure similar to that of $\text{Li}[\text{Li}_{1/6}\text{Al}_{1/6}\text{Mn}_{1/2}\text{Ni}_{1/6}]\text{O}_2$ reported by Dianat *et al.*,¹⁵ where they have taken $\text{Li}[\text{Li}_{1/6}\text{Mn}_{2/3}\text{Ni}_{1/6}]\text{O}_2$ as the base structure and all the transition elements are positioned in the LiM_2 layer. In this study, similar approach has been adopted with an incorporation of Co in the LiM_2 layer to generate different atomic configurations in the unit cell. Fig. 3 shows the highest and lowest formation energy (E_f) configurations of LNMC and these are referred as configuration 1 ($E_f = -23.52\text{ eV f.u.}^{-1}$) and configuration 2 ($E_f = -23.45\text{ eV f.u.}^{-1}$) respectively. In the configuration 1, both Ni and Li neighbour only with Mn and Co octahedra, whereas in configuration 2 the NiO_6 octahedron neighbours with the Li, Co and Mn octahedra and LiO_6 neighbours with the Ni, Co and Mn octahedra. A lower formation energy configuration (*i.e.* configuration 1) is considered further to evaluate the electrochemical properties. In the ESI† all other possible configurations have been given with their formation energies.

2.3 Phase analysis

Stability of different de-lithiated structures have been analysed by using the convex hull plot shown in Fig. 4. In the figure, the relative energy per formula unit (E_0) of most stable phases is connected ensuring that the curvature of the resulting arch always stays positive. For LMO, E_0 at $x = 2, 1.5, 1.25, 0.5, 0.25$, and 0 compositions lie on the curvature (Fig. 4a) and these are considered as stable phases. Phases with $x = 1.75$ and 1 stay within 3 meV above the line, which is below the typical accuracy of DFT calculations.²⁶ Therefore the phase can be considered as a stable phase. Although kinetic effects during cycling might prevent the phase to reach its lowest energy configuration, it would prefer to blend with the nearest neighbouring compositions of

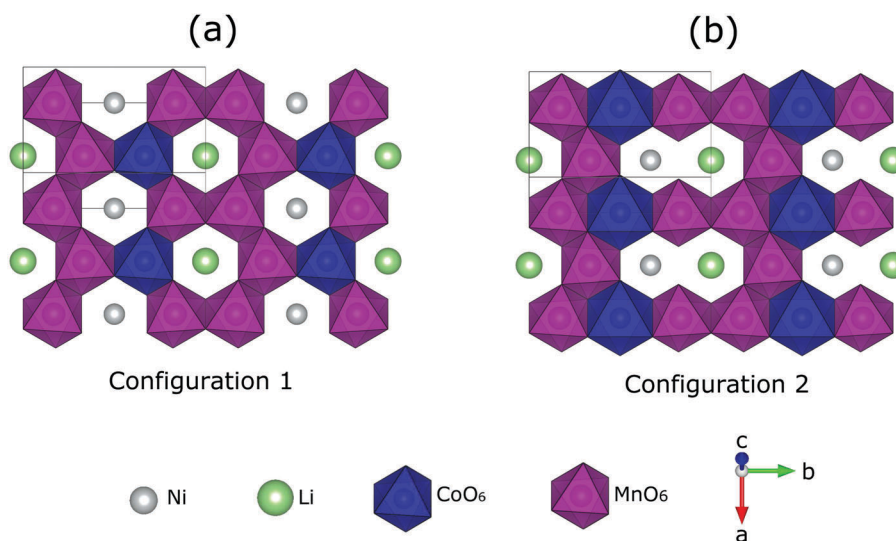


Fig. 3 (a) Possible atomic arrangements of 3d metals in the LiM_2 layer showing (a) the highest formation energy and (b) the lowest formation energy configurations of $\text{Li}_{1.17}\text{Ni}_{0.17}\text{Mn}_{0.5}\text{Co}_{0.17}\text{O}_2$.

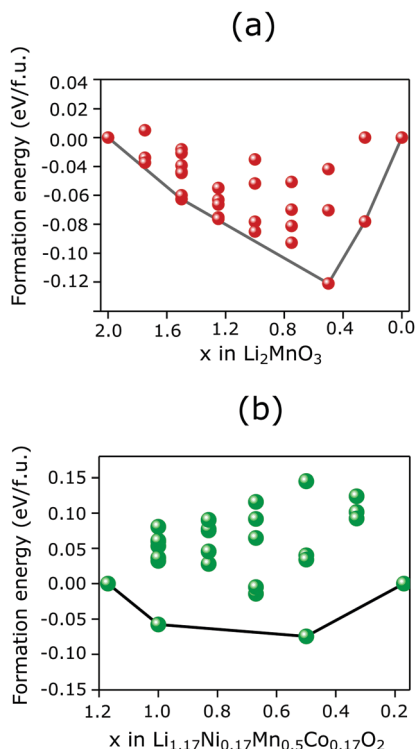


Fig. 4 Convex hull plot showing formation energy of different de-lithiated phases of (a) Li_2MnO_3 and (b) $\text{Li}_{1.17}\text{Ni}_{0.17}\text{Mn}_{0.5}\text{Co}_{0.17}\text{O}_2$.

the curvature. In the convex hull plot of LMO, an unstable phase is observed for $x = 0.75$ which stays above the line.

In the case of LNMC, relative energy of stable phases for the lithium concentration of $x = 1.2$, 1, 0.5, and 0.17 lies on the convex hull line (Fig. 4b). The bending of the convex hull is observed at $x = 0.5$, therefore it is considered as the most stable phase of LNMC, whereas unstable phases at $x = 0.85$, 0.67, and 0.33 stay above the line which suggests that two-phase reactions would take place in the region of $1 < x < 0.5$ and $0.5 < x < 0.17$. Consequently, voltage plateaus are observed in these two regions. Further details of the voltage profile are discussed in the subsequent section.

Based on the convex hull plot, a schematic of a lithium removal sequence is shown in Fig. 5. It can be seen from the figure that lithium is initially removed from the lithium layer and then from both the layers of lithium and LiM_2 . A similar sequence of Li-removal has been observed during the charge transfer process for other Li-rich compounds as well based on DFT calculations.²⁷ Although the sequence of Li-removal from specific sites is difficult to observe from experimental results, Mohanty *et al.*²⁸ have reported that Li is removed first from the Li-layer, and then from both the layers of Li and LiM_2 based on a change in c -lattice parameter with the help of *in situ* XRD analysis. Lithium removal from different layers affects the electrochemical potential and also the oxygen binding energy of the compound.²⁷

2.4 Voltage profile

In Fig. 6, a DFT calculated voltage profile along with experimental results of both the compounds have been compared. Voltage steps

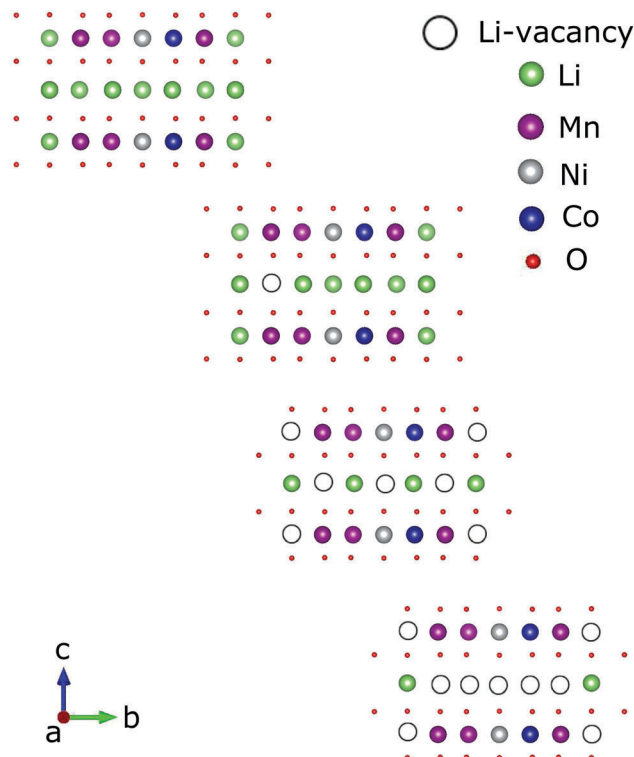


Fig. 5 Schematic showing the sequence of Li removal from the $\text{Li}_{1.17}\text{Ni}_{0.17}\text{Mn}_{0.5}\text{Co}_{0.17}\text{O}_2$ structure. Initial de-lithiation takes place from the lithium layer followed by the layers of LiM_2 and metals instantaneously.

in the calculated profile correspond to each arc of the convex hull plot. For LMO, a nearly flat voltage (4.6 V) step has been observed till $x = 1.25$ composition (Fig. 6a) as a change in relative energy from one stable phase to another is negligible. Also in the experimental voltage profile of LMO, a flat plateau has been observed at 4.6 V during the initial de-lithiation process. Xiao *et al.* also reported a de-lithiation potential of 4.6 V for LMO based on DFT calculations.²⁹ A current study has discussed electrochemical properties of LMO within a lithium concentration $x = 2$ to 1 considering deeper de-lithiation is practically difficult.

For LNMC significant differences have been observed in the voltage profile (Fig. 6b). In Fig. 6b, the first voltage step appears at 4.04 V with a change in compositions of $x = 1.17-1$. This corresponds to a single phase reaction. Subsequent voltage steps appear at 4.23 and 4.42 V with a change in $x = 1-0.5$ and $0.5-0.17$ respectively, where two phase reactions take place. Experimentally a steep slope is observed between 3.7–4.3 V and this corresponds to the oxidation of $\text{Ni}^{2+}/\text{Ni}^{4+}$ and $\text{Co}^{3+}/\text{Co}^{4+}$.³⁰ A steep slope in this voltage range suggests a single phase reaction.^{31,32} The flat plateau beyond 4.4 V corresponds to two phase reactions. In this region, lithium removal from the transition metal layer is accompanied by complex reactions involving oxygen loss and structural rearrangement.^{33,34}

2.5 Oxygen binding energy

In Fig. 7, oxygen binding energy of different de-lithiated phases of LMO and LNMC is compared along with previously reported

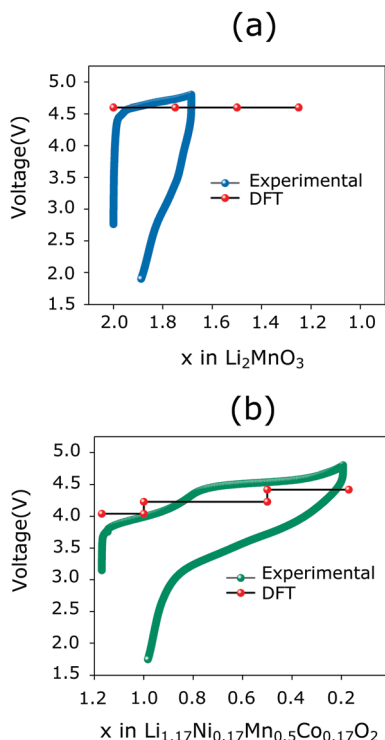


Fig. 6 Galvanostatic charge-discharge profile with a theoretically calculated voltage plot for (a) Li_2MnO_3 and (b) $\text{Li}_{1.17}\text{Ni}_{0.17}\text{Mn}_{0.5}\text{Co}_{0.17}\text{O}_2$.

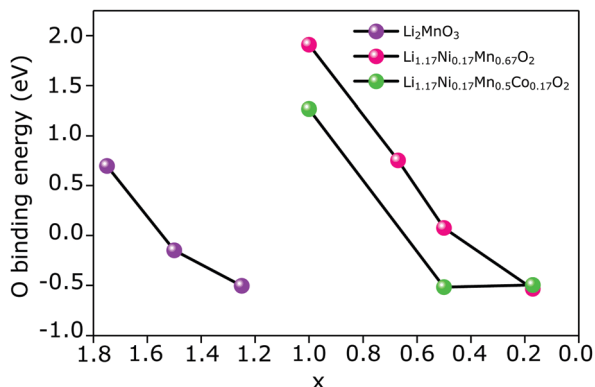


Fig. 7 Trend in oxygen binding energy as a function of Li concentration for Li_2MnO_3 , $\text{Li}_{1.17}\text{Mn}_{0.67}\text{Ni}_{0.17}\text{O}_2$ and $\text{Li}_{1.17}\text{Ni}_{0.17}\text{Mn}_{0.5}\text{Co}_{0.17}\text{O}_2$.

$\text{Li}_{1.17}\text{Ni}_{0.17}\text{Mn}_{0.67}\text{O}_2$ (LNMO).²⁷ The binding energy is calculated for the stable phases as appeared in the convex hull plot.

The oxygen binding energy of LMO at $x = 1.75$ is 0.7 eV, and it goes below 0 eV for further activation processes, whereas the binding energy increases in the Ni substituted material (LNMO).

On the other hand, the energy will reduce with incorporation of Co in LNMC. The oxygen binding energy in the Co substituted compound with lithium concentration at $x = 1$ is 1.26 eV and for the next stable phase (where $x = 0.5$), it is -0.52 eV.

The M–O bond dissociation energy (ΔH_f) suggests that the Mn–O ($\Delta H_f = 402 \text{ kJ mol}^{-1}$) and Ni–O ($\Delta H_f = 391.6 \text{ kJ mol}^{-1}$) bonds are stronger than the Co–O bond ($\Delta H_f = 368 \text{ kJ mol}^{-1}$).¹⁶ Therefore oxygen binding energy reduces with Co substitution in LNMC. Oxygen binding energy of both LMNO and LMNC (~ -0.53 eV) is nearly identical at deep de-lithiation state.

In the subsequent section, the partial density of states (PDOS) of transition metals and oxygen has been analysed to understand the origin of oxygen evolution in the studied compositions.

2.6 Charge transfer

To calculate lithium charge distribution, the Bader method has been used here. It helps to estimate the charge surrounding an atom x (Q_x). The difference of Q_x between lithiated and de-lithiated compound is used to calculate the lithium charge distribution on that atom x (B_x). Table 1 summarises lithium charge distribution of different atoms on the lithiated compound. For the charge distribution analysis of Li_2MnO_3 , LiMnO_3 is considered as a final de-lithiated compound. The analysis shows that O shares majority of lithium charge which is about 90% and Mn shares remaining 10%.

In the case of LNMC where lithium concentration in the final de-lithiated compound is $x = 0.17$, Li valence charge is mainly concentrated on O which is about 81.15%, however, it is reduced from that of LMO as Mn (11.04%), Co (3.73%) and Ni (4.08%) participate in a charge transfer process. This has been noticed for other layered oxide systems as well where Li valence charge mainly localized to oxygen p-orbitals.^{35–37}

2.7 Redox center and effective charge

To understand the redox center in the charge transfer process, CV analysis is presented along with effective charge calculations for different atoms. Furthermore, X-ray Photoelectron Spectroscopy (XPS) analysis (Fig. 8) has been conducted to confirm the oxidation states of transition metals in the parent phases.

Fig. 8a shows the wide spectra for LMO encompassing the signals for C 1s, Li 1s, Mn 2p, and O 1s. The core level spectrum for Mn 2p (Fig. 8b) appears at the binding energies of ~ 642 eV ($2p_{3/2}$) and 653 eV ($2p_{1/2}$). The deconvoluted Mn 2p spectrum indicates the presence of Mn^{4+} species.³⁸ Similarly, Fig. 8c displays the wide spectra of LNMC. Individual elemental spectra (Fig. 8d–f) are found at 854–869 eV, 779–794 eV and 642–653 eV

Table 1 Percentage of Li charge distribution among oxygen and metal atoms and change in effective charge of oxygen and metals for lithiated and de-lithiated compounds

Change in composition	Li valence charge distribution (%)				Change in effective charge (q)			
	Mn	Ni	Co	O	Mn	Ni	Co	O
Li_2MnO_3 – LiMnO_3	10.00			90.00	1.65/1.79			$-1.12/-0.86$
$\text{Li}_{1.17}\text{Ni}_{0.17}\text{Mn}_{0.5}\text{Co}_{0.17}\text{O}_2$ – $\text{Li}_{0.17}\text{Ni}_{0.17}\text{Mn}_{0.5}\text{Co}_{0.17}\text{O}_2$	11.04	4.08	3.73	81.15	1.69/1.87	1.2/1.4	1.52/1.71	$-1.14/-0.8$

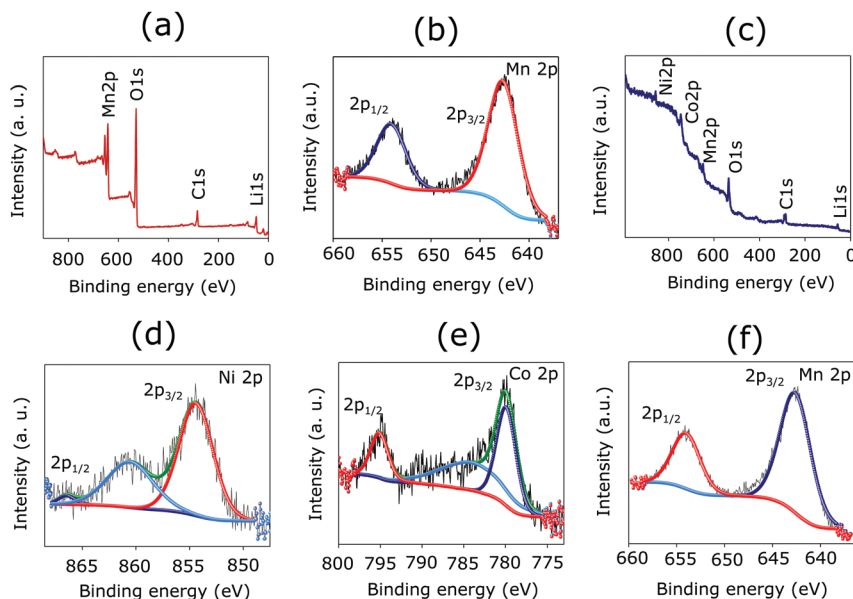


Fig. 8 (a) X-ray photoelectron survey spectrum of Li_2MnO_3 ; (b) core level spectrum of Mn 2p in Li_2MnO_3 ; (c) X-ray photoelectron survey spectrum of $\text{Li}_{1.17}\text{Ni}_{0.17}\text{Mn}_{0.5}\text{Co}_{0.17}\text{O}_2$ and its core level spectrum for (d) Ni 2p, (e) Co 2p and (f) Mn 2p.

which can be ascribed to Ni 2p, Co 2p, and Mn 2p core level spectrum, and their deconvolution indicates the presence of Ni^{2+} , Co^{3+} , and Mn^{4+} ions, respectively.³⁹ The envelopes of Li 1s, and O 1s core-level spectra for both the samples are depicted in the ESI† (Fig. S2). The Li 1s peak was observed at ~ 53.5 eV for both the samples and the peak at ~ 529 eV could correspond to the oxygen atoms in both the LMO and LNMC.

Fig. 9 shows the CV curves of LMO and LNMC. CV has been performed between 1.75 and 4.8 V (vs. Li/Li^+) at a sweep rate of 0.05 mV s^{-1} . In both the figures during the initial charging

process the sharp peak at around 4.6 V is attributed to the Li^+ extraction with a concurrent oxygen loss and structural rearrangement. The peak at ~ 3.3 V corresponds to the redox process of $\text{Mn}^{3+}/\text{Mn}^{4+}$. In Fig. 9b, peaks at ~ 3.7 V and ~ 4.3 V correspond to the redox process of $\text{Ni}^{2+}/\text{Ni}^{4+}$ and $\text{Co}^{3+}/\text{Co}^{4+}$ respectively.

Effective charge (q) calculation (Table 1) also confirms the redox centers for both the compounds. q is calculated after taking the difference between Q_x and number of valence electrons of x . For LMO the effective charge of Mn and O is changed from $+1.65e$ to $+1.79e$ and $-1.12e$ to $-0.86e$ respectively. It suggests that O is mainly redox active in the charge transfer process, whereas for LNMC a change in effective charge of Mn, Ni, Co and O is $+1.69e$ to $+1.87e$, $+1.2e$ to $+1.4e$, $+1.52e$ to $+1.71e$, and $-1.14e$ to $-0.8e$ respectively. This suggests that all are redox active and participate in a charge transfer process.

2.8 Density of states

To study the charge transfer mechanism and its electronic origin, the PDOS of Mn-d, Ni-d, Co-d, and O-p orbitals (Fig. 10) has been analysed for LMO and LNMC. For all the compositions oxygen p-orbital stays near to the Fermi energy and it dominates during a charge transfer process. This has been confirmed by the Bader analysis as well. For both the compounds there is no significant change in the Mn-d states.

The occupied Ni-d orbitals in LNMC are observed closer to the Fermi energy, which are oxidised on de-lithiation and at $x = 1$, it appears as an unoccupied orbital in the vicinity of the Fermi level. Co gets oxidised on further deep de-lithiation for $x = 0.5$ and unoccupied states of Co-d are observed near to the Fermi energy. This suggests that oxidation of Ni takes place followed by Co during de-lithiation of LNMC. CV analysis also confirms the sequence of redox centres in Co substituted LNMC.

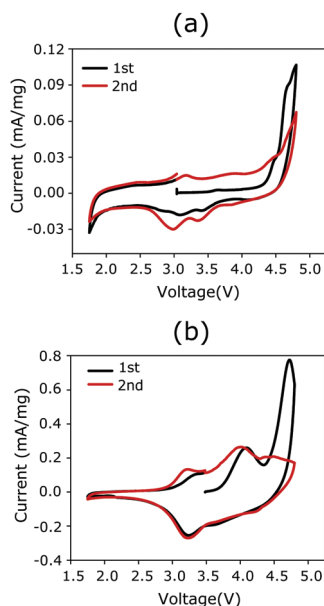


Fig. 9 Cyclic voltammetry of (a) Li_2MnO_3 and (b) $\text{Li}_{1.17}\text{Ni}_{0.17}\text{Mn}_{0.5}\text{Co}_{0.17}\text{O}_2$ at a scan rate of 0.05 mV s^{-1} in the potential window of 1.75–4.8 V.

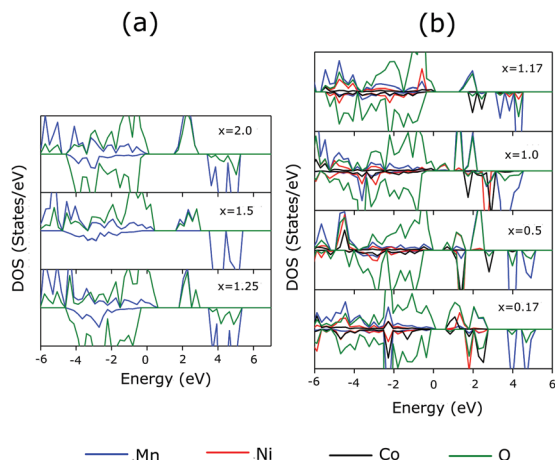


Fig. 10 Partial density of states of transition elements and oxygen for different compositions of (a) Li_2MnO_3 and (b) $\text{Li}_{1.17}\text{Ni}_{0.17}\text{Mn}_{0.5}\text{Co}_{0.17}\text{O}_2$.

O-p orbitals of LNMC shift near to the Fermi energy as compared to that of LMNO resulting in an easy electron transfer which facilitates O-removal from the structure.

At an early de-lithiation stage of LMO, more number of unoccupied O-p orbitals are located near to the Fermi energy as compared to LNMC. This triggered oxygen removal from the structure at the beginning of the charge transfer process in LMO as compared to LNMC.

3 Conclusion

The experimental and theoretical findings summarize the electrochemical performance of Li_2MnO_3 and $\text{Li}_{1.17}\text{Ni}_{0.17}\text{Mn}_{0.5}\text{Co}_{0.17}\text{O}_2$. DFT studies revealed that Ni and Li octahedra in the LiM_2 layer of LNMC are neighboured only with Mn and Co octahedra. Furthermore, it indicated that the de-lithiation of LNMC resulted in two-phase reactions in the region of $1 < x < 0.5$ and $0.5 < x < 0.17$, and subsequently a voltage plateau was observed at 4.23 V and 4.42 V. This matches well with the experimental observation. Experimentally a two-phase reaction has been observed at a voltage of 4.5 V. The DFT calculations also revealed a charge transfer mechanism wherein the incoming Li charge is mainly localized on O for both LMO and LNMC. In LMO, the presence of more number of unoccupied O-p orbitals near to the Fermi energy helps in the faster removal of O compared to LNMC. With the substitution of Co, an unoccupied O-p orbital shifts towards the Fermi energy as compared to LMNO resulting in the removal of O during the initial activation period. DFT studies analyse the sequence of redox centers while de-lithiation takes place. With the removal of Li in LNMC, the unoccupied Ni-d orbital is determined in the vicinity of the Fermi level followed by unoccupied states of Co-d orbitals, which confirms the sequence of redox center, Ni followed by Co. CV analysis also suggests the oxidation of Ni^{2+} before Co^{3+} . This study examined the charge transfer mechanism and oxygen removal in Li-rich cathode materials and discussed the role of transition metals and oxygen.

Conflicts of interest

There are no conflicts to declare.

Acknowledgements

Mr K. R. Prakasha thanks UGC for JRF/SRF Fellowship. The authors thank the Central Instrumentation Facility, CSIR-CECRI, Karaikudi. This work was supported by Department of Science and Technology, Science and Engineering research board, New Delhi, under the grant scheme "Clean Energy Research Initiative" (Grant No. DST/TMD/CERI/C16).

References

- 1 J. S. Kim, C. S. Johnson, J. T. Vaughey, M. M. Thackeray, S. A. Hackney, W. Yoon and C. P. Grey, *Chem. Mater.*, 2004, **16**, 1996–2006.
- 2 M. M. Thackeray, C. S. Johnson, J. T. Vaughey, N. Li and S. A. Hackney, *J. Mater. Chem.*, 2005, **15**, 2257–2267.
- 3 M. M. Thackeray, S. Ho Kang, C. S. Johnson, J. T. Vaughey, R. Benedeka and S. A. Hackney, *J. Mater. Chem.*, 2007, **17**, 3112–3125.
- 4 T. Ohzuku, M. Nagayama, K. Tsuji and K. Ariyoshi, *J. Mater. Chem.*, 2011, **21**, 10179–10188.
- 5 F. Amalraj, D. Kovacheva, M. Talianker, L. Zeiri, J. Grinblat, N. Leifer, G. Goobes, B. Markovsky and D. Aurbach, *J. Electrochem. Soc.*, 2010, **157**, A1121–A1130.
- 6 D. Im, J. Kim, J. Yoon, K.-S. Park, Y.-G. Ryu, S. S. Lee, D. J. Lee and S.-G. Doo, *ECS Meeting Abstracts*, 2010, MA2010-01, 630.
- 7 M. N. Ates, Q. Jia, A. Shah, A. Busnaina, S. Mukerjee and K. M. Abraham, *J. Electrochem. Soc.*, 2014, **161**, A290–A301.
- 8 M. Gu, I. Belharouak, J. Zheng, H. Wu, J. Xiao, A. Genc, K. Amine, S. Thevuthasan, D. R. Baer, J.-G. Zhang, N. D. Browning, J. Liu and C. Wang, *ACS Nano*, 2013, **7**, 760–767.
- 9 L. Eunseok and K. A. Persson, *Adv. Energy Mater.*, 2014, **4**, 1400498.
- 10 M. Saubanere, E. McCalla, J.-M. Tarascon and M.-L. Doublet, *Energy Environ. Sci.*, 2016, **9**, 984–991.
- 11 S. Kim, M. Aykol, V. I. Hegde, Z. Lu, S. Kirklin, J. R. Croy, M. M. Thackeray and C. Wolverton, *Energy Environ. Sci.*, 2017, **10**, 2201–2211.
- 12 Y. Xie, M. Saubanere and M.-L. Doublet, *Energy Environ. Sci.*, 2017, **10**, 266–274.
- 13 W. E. Gent, K. Lim, Y. Liang, Q. Li, T. Barnes, S.-J. Ahn, K. H. Stone, M. McIntire, J. Hong, J. H. Song, Y. Li, A. Mehta, S. Ermon, T. Tylliszczak, D. Kilcoyne, D. Vine, J.-H. Park, S.-K. Doo, M. F. Toney, W. Yang, D. Prendergast and W. C. Chueh, *Nat. Commun.*, 2017, **8**, 2091.
- 14 C. P. Laisa, A. K. Nanda Kumar, S. Selva Chandrasekaran, P. Murugan, N. Lakshminarasimhan, R. Govindaraj and K. Ramesha, *J. Power Sources*, 2016, **324**, 462–474.
- 15 A. Dianat, N. Seriani, M. Bobeth and G. Cuniberti, *J. Mater. Chem. A*, 2013, **1**, 9273–9280.

- 16 Z. Q. Deng and A. Manthiram, *J. Phys. Chem. C*, 2011, **115**, 7097–7103.
- 17 P. Xiao, Z. Q. Deng, A. Manthiram and G. Henkelman, *J. Phys. Chem. C*, 2012, **116**, 23201–23204.
- 18 R. F. W. Bader, *Atoms in molecules, Encyclopedia of computational chemistry*, 2002.
- 19 G. Kresse and D. Joubert, *Phys. Rev. B: Condens. Matter Mater. Phys.*, 1999, **59**, 1758–1775.
- 20 J. P. Perdew, K. Burke and M. Ernzerhof, *Phys. Rev. Lett.*, 1996, **77**, 3865–3868.
- 21 H. J. Monkhorst and J. D. Pack, *Phys. Rev. B: Solid State*, 1976, **13**, 5188–5192.
- 22 G. Ceder, M. Aydinol and A. Kohan, *Comput. Mater. Sci.*, 1997, **8**, 161–169.
- 23 Z. Lu, L. Y. Beaulieu, R. A. Donaberger, C. L. Thomas and J. R. Dahn, *J. Electrochem. Soc.*, 2002, **149**, A778–A791.
- 24 A. Rougier, P. Gravereau and C. Delmas, *J. Electrochem. Soc.*, 1996, **143**, 1168–1175.
- 25 P. Strobel and B. Lambert-Andron, *J. Solid State Chem.*, 1988, **75**, 90–98.
- 26 S. Loftager, J. M. Garcia-Lastra and T. Vegge, *J. Phys. Chem. C*, 2016, **120**, 18355–18364.
- 27 T. Sarkar, K. R. Prakasha, M. D. Bharadwaj and A. S. Prakash, *J. Phys. Chem. C*, 2017, **121**, 20591–20596.
- 28 D. Mohanty, S. Kalnaus, R. A. Meisner, K. J. Rhodes, J. Li, E. A. Payzant, D. L. Wood III and C. Daniel, *J. Power Sources*, 2013, **229**, 239–248.
- 29 R. Xiao, H. Li and L. Chen, *Chem. Mater.*, 2012, **24**, 4242–4251.
- 30 W. Liu, G. Fang, B. Xia, H. Sun, S. Kaneko and D. Li, *RSC Adv.*, 2013, **3**, 15630–15635.
- 31 A. Van der Ven, J. Bhattacharya and A. A. Belak, *Acc. Chem. Res.*, 2013, **46**, 1216–1225.
- 32 D. Li and H. Zhou, *Mater. Today*, 2014, **17**, 451–463.
- 33 J.-M. Kim, N. Kumagai and H.-T. Chung, *Electrochem. Solid-State Lett.*, 2006, **9**, A494–A498.
- 34 K. R. Prakasha and A. S. Prakash, *RSC Adv.*, 2015, **5**, 94411–94417.
- 35 W.-S. Yoon, K.-B. Kim, M.-G. Kim, M.-K. Lee, H.-J. Shin, J.-M. Lee, J.-S. Lee and C.-H. Yo, *J. Phys. Chem. B*, 2002, **106**, 2526–2532.
- 36 A. K. Varanasi, A. Bhowmik, T. Sarkar, U. V. Waghmare and M. D. Bharadwaj, *Ionics*, 2014, **20**, 315–321.
- 37 M. K. Aydinol, A. F. Kohan, G. Ceder, K. Cho and J. Joannopoulos, *Phys. Rev. B: Condens. Matter Mater. Phys.*, 1997, **56**, 1354.
- 38 J. Lim, J. Moon, J. Gim, S. Kim, K. Kim, J. Song, J. Kang, W. B. Ima and J. Kim, *J. Mater. Chem.*, 2012, **22**, 11772–11777.
- 39 K. R. Prakasha, M. Sathish, P. Bera and A. S. Prakash, *ACS Omega*, 2017, **2**, 2308–2316.